ARTICLE

Anion Defects Engineering of Ternary Nb-Based Chalcogenide Anodes Toward High-Performance Sodium-Based Dual-Ion Batteries

Yangjie Liu[1,2], Min Qiu[2,3], Xiang Hu[1,2], Jun Yuan[1,2], Weilu Liao[2], Liangmei Sheng[4], Yuhua Chen[4], Yongmin Wu[4], Hongbing Zhan[1] ✉, Zhenhai Wen[2] ✉

HIGHLIGHTS

- We developed an efficient and extensible strategy to produce the single-phase ternary NbSSe nanohybrids with defect-enrich micro-structure.

- The anionic-Se doping play a key role in effectively modulating the electronic structure and surface chemistry of NbS_2 phase, including the increased interlayers distance (0.65 nm), the enhanced intrinsic electrical conductivity (3.23×10^3 S m^{-1}) and extra electroactive defect sites.

- The NbSSe/NC composite as anode exhibits rapid Na+ diffusion kinetics and increased capacitance behavior for Na$^+$ storage, resulting in high reversible capacity and excellent cycling stability.

ABSTRACT Sodium-based dual-ion batteries (SDIBs) have gained tremendous attention due to their virtues of high operating voltage and low cost, yet it remains a tough challenge for the development of ideal anode material of SDIBs featuring with high kinetics and long durability. Herein, we report the design and fabrication of N-doped carbon film-modified niobium sulfur–selenium (NbSSe/NC) nanosheets architecture, which holds favorable merits for Na$^+$ storage of enlarged interlayer space, improved electrical conductivity, as well as enhanced reaction reversibility, endowing it with high capacity, high-rate capability and high cycling stability. The combined electrochemical studies with density functional theory calculation reveal that the enriched defects in such nanosheets architecture can benefit for facilitating charge transfer and Na$^+$ adsorption to speed the electrochemical kinetics. The NbSSe/NC composites are studied as the anode of a full SDIBs by pairing the expanded graphite as cathode, which shows an impressively cyclic durability with negligible capacity attenuation

over 1000 cycles at 0.5 A g^{-1}, as well as an outstanding energy density of 230.6 Wh kg^{-1} based on the total mass of anode and cathode.
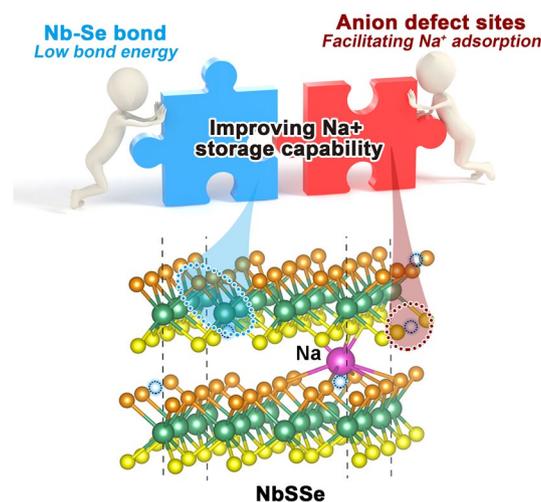
✉ Hongbing Zhan, hbzhan@fzu.edu.cn; Zhenhai Wen, wen@fjirsm.ac.cn
1 College of Materials Science and Engineering, Fuzhou University, Fuzhou 350108, People's Republic of China
2 CAS Key Laboratory of Design and Assembly of Functional Nanostructures, and Fujian Provincial Key Laboratory of Materials and Techniques Toward Hydrogen Energy, Fujian Institute of Research on the Structure of Matter, Chinese Academy of Sciences, Fuzhou, Fujian 350002, People's Republic of China
3 Fujian Normal University, Fuzhou 350108, People's Republic of China
4 State Key Laboratory of Space Power-Sources Technology, Shanghai Institute of Space Power Sources, 2965 Dongchuan Road, Shanghai 200245, People's Republic of China

1 Introduction

Sodium-based dual-ion batteries (SDIBs) have become emerging techniques with potential application in the fields of energy storage thanks to their various advantages, such as high output voltage and the rich sodium resource, as well as environmental compatibility of nontransition-metal cathode [1, 2]. However, the larger size of Na$^+$ (0.102 nm vs. Li$^+$ 0.076 nm) leads to slow kinetics of ion transport and huge volumetric variation of anode during sodiation/desodiation process [3]. Graphite, as the commercial anodes of lithium-ion battery, yet is not fit for Na$^+$ storage due to the low reversible Na$^+$ storage capacity (around 30 mAh g^{-1} for NaC$_{64}$) [4, 5]. Therefore, it is vitally important to explore appropriate materials to meet the requirement of Na$^+$ storage.

As a typical transition-metal chalcogenide, niobium disulfide (NbS$_2$) has been regarded as a prospective candidate as it has a well-defined layered structure with large lattice spacing (0.62 nm), high theoretical specific capacity (683 mAh g^{-1}) and a rather preferable electrical conductivity (1×10^3 S m^{-1}) [6]. However, the bulk NbS$_2$ for Na$^+$ storage faces several key challenges, including the poor accessibility of active sites and the slow inferior electron/ion conductivity, which has a limited capacity and sluggish kinetic [7]. In addition, NbS$_2$ tends to agglomerate and pulverize, and the severe volume variation upon the de-/sodiation process that finally results in rapid capacity degradation and inferior cycling capability. To settle these issues, some researchers have reported that the optimization of component and microstructure can effectively enhance electrochemical performance of anode [8]. Although appreciable progress has been made, the conversion reaction kinetics of NbS$_2$ electrode is still restricted by the intrinsic high reaction energy barriers due to high bond dissociation energy barrier of Nb–S bonds (> 320 kJ mol^{-1}) [9, 10].

Recently, the anion defect engineering has been regarded as an effective route to improve the electrochemical activity of nanomaterials upon discharging/charging process: (1) The electrons in the defect sites can be stimulated into the conduction band, producing a narrowing of the bandgap which is conducive to enhancing the charge transfer dynamics; (2) moreover, the anion defects would modify the local electronic properties of adjacent atoms, thus leading to reduce the decomposition activation energy

of intermediate and improve the efficiency of conversion reaction [11, 12]. Selenium (Se) presents a similar physicochemical character to sulfur (S), while it has a larger atomic size and lower electronegativity. Thus, the in situ doping of Se into the lattice of NbS$_2$ should be a viable route to create anion defect sites and to improve the conductivity [13, 14]. In addition, the relative low bond dissociation energy of Nb–Se to Nb–S favors the reversible conversion reaction for improving the reversibility, which benefits for enhancing the capability to store Na$^+$ and expediting the reaction kinetics [4, 15]. However, the incorporation of anion defects into the NbS$_2$ anode has never been reported; and also, the scientific understanding of the defect structure–performance relationship on Na$^+$ storage behavior needs to be further in-depth studied.

Herein, we report the synthesis of single-phase NbSSe nanoarchitecture hybrids (NbSSe/NC) with N-doped carbon film decorating few-layer sheets as building blocks. Such NbSSe/NC nanosheets architecture with S–Nb–Se interlayer ligands combines the desired merits of few-layered structure with expanded interlayer space, improved electrical conductivity and defect-enriched microstructure. Accordingly, the NbSSe/NC nanohybrids exhibit highly impressive electrochemical properties toward sodium-ion storage with high specific capacity and long-term durability, which prompt us to develop a high-performance sodium-based dual-ion battery with high energy density and long-term durability.

2 Experimental Section

2.1 Chemicals

All the reagents were directly used without further purification. Niobium chloride (NbCl$_5$, 99.9%) and selenium powder (Se, ≥ 99.99% metals basis) were purchased from Shanghai Macklin Biochemical Co., Ltd.; 1-octadecene (ODE, 90%) and oleylamine (OA, 98%) were purchased from Adamasbeta; and carbon disulfide (CS$_2$, Aldrich, 99.9%) was from Sinopharm Chemical Reagent Co., Ltd. All chemicals were used without further purification.

2.2 Synthesis

2.2.1 Synthesis of NbS₂–OA

First, 250 mg $NbCl_5$, 10 mL of OA and 10 mL ODE were mixed in a three-neck flask. The mixture was degassed under a vacuum for 20 min at room temperature to remove H_2O and O_2 and then heated to 140 °C for 30 min under argon atmosphere protection. Subsequently, the solution was further heated 280 °C with a heating rate of 5 °C min^{-1}. While heating, the orange color was turned to light brown. Once the system reached 280 °C, 3 mL CS_2 solution was slowly injected into the flask. After injection, the reaction temperature was maintained at 280 °C for 60 min. After that, the brown precipitates (NbS_2–OA) were collected by centrifugation, washed with *n*-hexane and methanol for several times and vacuum-dried at 70 °C for one night. The NbS_2 was obtained in the same way as NbS_2–OA without adding the OA.

2.2.2 Synthesis of NbSSe/NC, NbS₂/NC and NbS₂

To prepare the NbSSe/NC composites, the NbS_2–OA precursor and selenium powder were mixed with a molar ratio of S:Se (1:1), and then, the mixture was heated at 500 °C for 2 h in a sealed glass bottle under H_2/Ar protection. For comparison, the NbS_2/NC composite was prepared in the same way as NbSSe/NC, just without selenium powder; the NbS_2 composite was prepared in the same way as NbS_2/NC, just without OA.

2.3 Characterization

The morphologies of materials were characterized by FESEM (Hitachi SU-8020) and HRTEM (Tecnai F20). The structure and composition of products were measured by XPS (ESCALAB 250Xi, Thermo Fisher), XRD (Miniflex 600 powder X-ray diffractometer with Cu Kα radiation in the 2θ range from 10° to 70°) and Raman spectrum (LabRam HR800). The electronic conductivity was tested by a four-point probe method at the current of 0.02 mA (RTS-8, 4Probes Tech Ltd.). EPR spectra were recorded using a Bruker spectrometer (ELEXSYS E500).

The specific surface area was performed using the Brunauer–Emmett–Teller equation by nitrogen adsorption and desorption isotherm (IGA100B). TGA test of the samples was performed by a simultaneous thermal analyzer (STA 449 F3 Jupiter, NETZSCH).

2.4 Electrochemical Measurements

2.4.1 Anode and Cathode Preparation

The negative electrodes consisted of the 80 wt% active materials (NbSSe/NC, NbS_2/NC, or NbS_2), 10 wt% Ketjen Black and 10 wt% carboxyl methyl cellulose (CMC) binder onto Cu foil. The loading mass of anode was maintained at about 1.2 ~ 1.5 mg cm^{-2}. The electrochemical measurements were investigated with 2032-type coin cells assembled in a glove box filled with argon atmosphere (< 0.5 ppm of H_2O and O_2).

2.4.2 For the Half-cell

The metallic Na foil was used as the counter and reference electrodes, the glass fiber (Whatman) as the separator film and 1 M $NaPF_6$ dissolved in ethylene carbonate/ethyl methyl carbonate/dimethyl carbonate (EC/EMC/DMC, 1:1:1, v/v/v), and 7% FEC was used as the electrolyte. The electrolyte/active material ratio in each cell was ~ 100 µL mg^{-1}. The specific capacity and specific currents were calculated based on the weight of anode materials.

2.4.3 For the Sodium-based Dual-ion Full Cell

The preparation method of EG cathode was same with anode, just employing the polyvinylidene fluoride (PVDF) as binder and Al foils as current collector. The areal loading of EG cathode was about 5 ~ 6 mg cm^{-2}. The mass ratio of anode to cathode was preset to about 1:4. The electrolyte was the 3 M $NaPF_6$ in the solution of EC/EMC/DMC and 7% FEC. The cyclic voltammetry (CV) curves were measured by a CHI660E electrochemical workstation. The galvanostatic charge/discharge (GCD) cycling and rate capability tests were conducted on a Neware battery test system (CT-ZWJ-4'S-T-1U, Shenzhen, China) with the voltage range of 0.01–3 V for SIBs and 1.5–4.8 V for SDIBs. For the long-term cycling performance at high rate, the SDIBs were first

activated at 0.1 A g^{-1} for ten cycles and then were operated at a higher specific current for a long cycle test. An ac voltage amplitude of 5.0 mV was employed to measure EIS within the frequency range from 10 mHz to 100 kHz.

2.5 Calculation Method

The DFT calculations were performed with periodic supercells under the generalized gradient approximation (GGA) using the Perdew–Burke–Ernzerhof (PBE) function for exchange–correlation and the ultrasoft pseudopotentials for nuclei and core electrons. The Kohn–Sham orbitals were expanded in a plane-wave basis set with a kinetic energy cutoff of 30 Ry and the charge density cutoff of 300 Ry. The adsorption energy ΔE_a can be calculated by Eq. 1:

$$\Delta E_a = E_{tot} - E_{Na} - E_{str} \tag{1}$$

where E_{tot} is the total energy of compound obtained from DFT calculations, E_{Na} is the energy of Na atoms and E_{str} is the energy of each structure. Electron density difference was calculated by subtracting the charge densities of Na atom and each configuration from the corresponding compounds. The charge density difference can be used to analyze the bonding process or the charge transfer before and after structural relaxation. The charge density difference of system can be calculated by Eq. 2:

$$\Delta\rho = \rho_{AB} - \rho_A - \rho_B \tag{2}$$

where ρ_{AB} is the composition, ρ_A is the base and ρ_B is the absorbate. In calculation of the latter two quantities, the atomic positions are fixed as those they have in the AB system. The Fermi surface effects have been treated by the smearing technique of Methfessel and Paxton, using a smearing parameter of 0.02 Ry. The Brillouin zones were sampled with a k-point with gamma point. A supercell of $3 \times 3 \times 1$ is adopted. The diffusion barrier for Na atom was determined by nudged elastic band (NEB). All the DFT calculations are implemented by the PW and NEB modules contained in the Quantum ESPRESSO distribution.

3 Results and Discussion

3.1 DFT Analysis of the Effect of Se Dopants on Na$^+$ Storage

Figure 1a presents the difference of the basal plane activation in active electronic states between NbS$_2$ and NbSSe.

The lower d-band center in NbS$_2$ leads to weak chemical reactivity with Na$^+$. The introducing of Se atoms into NbS$_2$ crystal lattice favors to introduce a charge self-regulation effect because the activated d orbital of Nb and p orbital of S across the Fermi surface in NbSSe structure, effectively accelerating the electron transfer during the electrochemical process. In addition, the generation of anion defects would provide rich active defect sites for contributing the surface pseudocapacitive capacity for Na$^+$ storage and fast kinetics.

Furthermore, the first-principles calculations were done to study the structural advantage of NbSSe for Na$^+$ storage. The optimized computational models with Se doping are depicted in Figs. 1b and S1–S2. The computation of average adsorption energy (ΔE_a) demonstrates that defect-enriched NbSSe structure displays stronger adsorption of Na ions by lower adsorption energy ($-2.29, -3.98$ and -5.64 eV), whereas the corresponding values for NbS$_2$ are $-1.64, -3.14$ and -4.67 eV, which implies the defect sites would provide effective adsorption for the increased surface-induced pseudocapacitive charge storage (Fig. S3) [16]. Figure 1c presents the electron density difference models for the adsorption of Na atoms on the surface of samples, while Fig. 1d is a slice of Fig. 1c. They show that defect-rich structured NbSSe would induce obvious interfacial charge redistribution compared to the defect-free NbS$_2$, indicative of a stronger interaction between Na and surface materials, leading to higher redox reaction activity [17]. The crystal orbital Hamilton population (COHP) analysis is performed to study the interaction of Nb–S bond in NbS$_2$ and NbSSe (Fig. 1e). We found the integrated COHP (ICHOP, -0.674 eV) value of NbS$_2$ is significantly smaller than that of NbSSe (-0.129 eV) near the Fermi level, which implies the introduction of selenium ions would make Nb–S bond easier to trigger the redox reaction, resulting in more kinetically favorable and higher electrochemical reversibility [18]. Therefore, the coupling of the anion defect construction and charge self-regulation effect can availably improve Na$^+$ adsorption and migration ability, therefore theoretically verifying the enhanced Na$^+$ storage property.

3.2 Synthesis and Characterizations of the NbSSe/NC

For the purpose of demonstrating our concept, the Se-doped NbS$_2$ nanohybrid electrode is prepared, as schematically
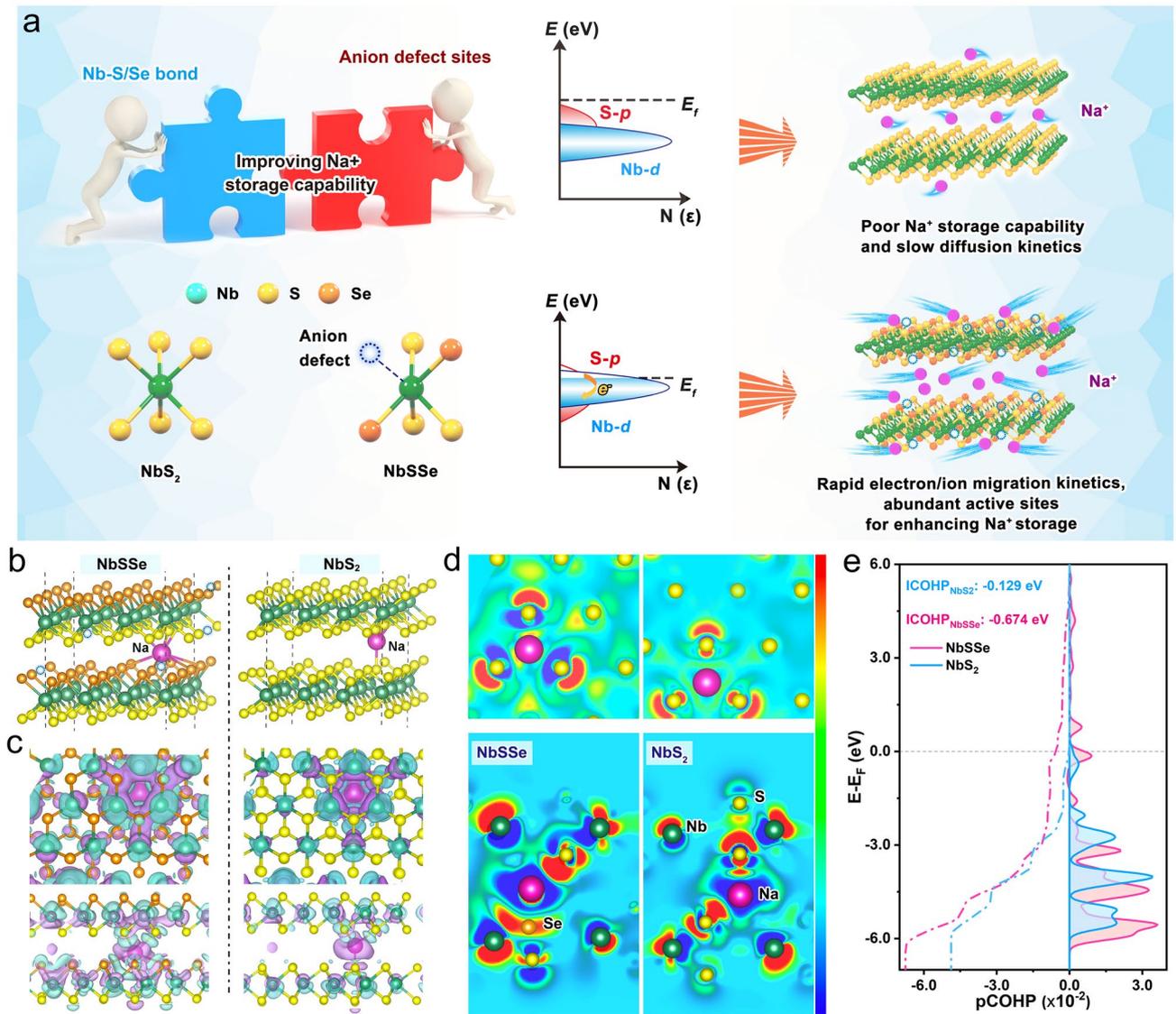
Fig. 1 **a** Schematic illustration of charge self-regulation effect on manipulating active electronic states. **b** The optimized structures of NbSSe and NbS$_2$ for Na$^+$ adsorption. **c** 3D electron density difference distribution and **d** cross-sectional diagram of intercalated Na in NbS$_2$ and NbSSe. **e** Average pCOHP and the corresponding integral patterns for NbS$_2$ and NbSSe

illustrated in Fig. 2a. NbCl$_5$ as the precursor was added into the hot bath composed of oleylamine (OA) and 1-octadecene (ODE) under an argon atmosphere to form the coordination complex of niobium chloro oleylamine (NbCl–OA) [19]; the mixture was then heated to 280℃ followed by slow injection of CS$_2$ for assembling into OA-modified NbS$_2$ nanospheres (NbS$_2$–OA) (Fig. S4), which was finally evolved into NbSSe composite through selenization process upon annealing, during which the OA was carbonized into N-doped carbon layer (denoted as NbSSe/NC).

Figure 2b exhibits field-emission scanning electron microscopy (FESEM) images of the NbSSe/NC nanohybrids, which display the nanoflower-like architecture with an average size of 800~900 nm with numerous two-dimensional building blocks of nanosheets. The transmission electron microscopy (TEM) and high-resolution TEM were conducted to study the fine structure. As shown in Figs. 2c and S5, one can observe that the NbSSe nanosheets are in the few-layer structure (2–4 layers), showing an expended interlayer distance of 0.65 nm, which is larger than the (002)

crystalline planes that of NbS_2 (0.61 nm). For comparison, the NbS_2/NC composite was also prepared by direct calcination of the NbS_2–OA precursor, which displayed a similar structure with NbSSe (Fig. S6), while for pure NbS_2, their nanosheets tended to agglomerate and failed to form nano-flower morphology (Fig. S7). More importantly, as shown in Fig. 2d, the atomic resolution images and the related fast Fourier transformation (FFT)-filtered pictures were utilized to visualize the NbSSe/NC and NbS_2/NC composites at a sub-angstrom resolution, which suggested obvious internal defects in the NbSSe basal plane; while for NbS_2/NC, a ordered hexagonal atomic lattice can be observed. The energy-dispersive spectroscopy (EDS) and corresponding mapping images showed uniform distribution of Nb, S, Se, C and N elements with the Se/S atomic ratio of ~ 1:1 (Figs. 2e and S8). These results indicate the Se atoms doping in NbS_2 lattice can effectively enlarge interlayer spacing and generate rich defects.

Figure 2f displays the X-ray diffraction (XRD) patterns of the NbSSe/NC; all characteristic peaks can be well indexed to NbSSe phase (JCPDS #40-1002), which is similar to the hexagonal crystal structure of NbS_2 (JCPDS No. 38-1367) [7]. Notably, the (002), (102) and (110) planes of the NbSSe/NC present an obvious negative shift to lower degree, implying an enlarged interlayer space induced by the introduction of large-sized Se atoms into NbS_2, which is in accordance with the TEM observation. To further confirm the phase evolution from NbS_2 to NbSSe, the Raman measurement was further carried out (Fig. S9). Two distinct characteristic peaks detected at ~ 370.2 and ~ 440.3 cm^{-1} in the NbS_2 sample are attributed to the in-plane E_{2g} vibration and out-plane A_{1g} vibration modes of Nb–S band, respectively [20]. As for the NbSSe/NC sample, both Nb–S modes shift negatively to the low-frequency range compared with NbS_2/NC, indicating the decreased symmetry of Nb–S bonds due to Se doping, and the formation of Nb–Se bond can be detected by the Nb–Se vibration at a wave number of 312.9 cm^{-1} [21]. The inductively coupled plasma result (ICP) reveals the elemental ratio of Nb:S is 1:1.95 for NbS_2/NC sample (Table S1), which is very close to the expected stoichiometry value. The elemental ratio among Nb, S and Se in NbSSe/NC is 1:0.9:0.9, which indicates the successful substitution of S with Se. The defects structure was further studied by electron paramagnetic response (EPR), as shown in Fig. 2g. The NbSSe/NC exhibits a couple of conspicuous peaks near a g-factor

of 2.003, which almost show one order magnitude higher than that of NbS_2/NC. This indicates the anion substitution of S by Se can generate abundant structure defects in NbS_2 lattice, which endows electrode materials with rich active sites and improved electrical conductivity, consequently conducting to the rapid charge carrier transport.

X-ray photoelectron spectroscopy (XPS) spectra were measured and utilized for analyzing the surface states of NbS_2-based nanomaterials. The survey XPS spectrum indicates the coexistence of Nb, S, Se, N and C elements (Fig. S10). Figure S11 shows the high-resolution Nb $3d$ spectrum of NbSSe/NC and NbS_2/NC samples, in which one can observe two peaks at ~ 207.0 and ~ 204.5 eV relating to the chemical environment of $3d_{3/2}$ and $3d_{5/2}$ of Nb^{4+}, respectively, accompanied with a pair of shoulder peaks at ~ 211.1 and ~ 208.3 eV referring to Nb^{5+} [22, 23]. As shown in the S $2p$ and Se $3p$ high-resolution XPS spectrum (Fig. 2h), the spectra can be deconvoluted into four peaks, where a pair of peaks at 162.8 eV and 164.5 eV are attributed to $2p_{3/2}$ and $2p_{1/2}$ of S^{2-}, and others at 161.7 and 165.8 eV belong to Se $2p_{3/2}$ and Se $2p_{1/3}$, respectively [24, 25]. Compared with that of NbS_2/NC sample, the characteristic peaks of both Nb $3d$ and S $2p$ for the NbSSe/NC show a negative migration (~ 0.9 eV) toward lower binding energies, which are assigned by the less electronegative chemical environment due to the incorporation of Se^{2-} into NbS_2 crystal lattice, thus decreasing energy binding of Nb–S. For the Se $3d$ spectra of NbSSe/NC (Fig. S12), two typical peaks are centered at 55.5 and 54.8 eV, corresponding to valence feature of Se^{2-} (Nb–Se) [26]; the peak at 56.3 eV could be assigned to the formation of Se–C bonds [27]. Moreover, the existence of Se–C bonds also could be detected from the C $1s$ spectrum (Fig. S13), which indicate interface coupling between NbSSe nanosheets and carbon layer, ensuring the reinforced electrical conductivity and the structural stability of composites. The high-resolution N $1s$ spectrum suggests the doping of N atoms into the carbon layer with fitting peaks at 402.6 eV (graphitic-N), 400.1 eV (pyrrolic-N) and 399.4 eV (pyridinic-N), as shown in Fig. S14 [28]. Furthermore, the electric conductivities of NbSSe/NC and NbS_2/NC composites were measured via a four-point probe method (Fig. S15). The NbSSe/NC exhibited a significantly enhanced electronic conductivity of 3.23×10^3 S m^{-1} relative to that (1.12×10^3 S m^{-1}) of NbS_2/NC, verifying the introduction of Se atoms endows NbS_2 with high electrical conductivity [29]. The carbon
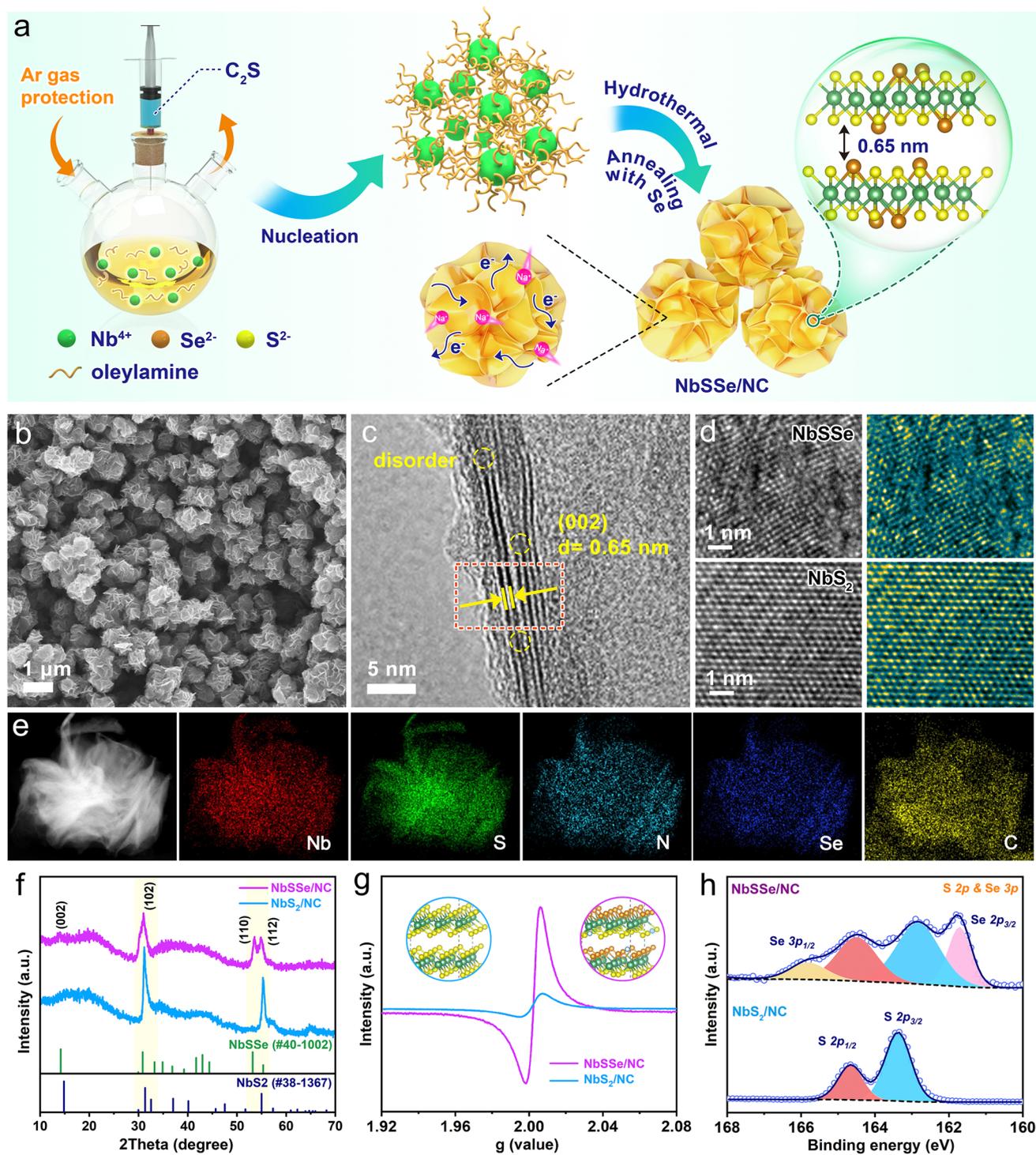
Fig. 2 **a** Schematic strategy of synthesis for the NbSSe/NC composites. **b** SEM images and **c** HRTEM images of NbSSe/NC, **d** atomic resolution pictures of NbSSe/NC and NbS₂/NC composites and related FFT-filtered atomic resolution images, **e** elemental mapping images of NbSSe/NC, **f** XRD pattern, **g** EPR results, **h** S $2p$ and Se $3p$ high-resolution XPS spectrum of NbSSe/NC and NbS₂/NC

content in NbSSe/NC was measured to be ~ 9.82% according to the thermogravimetric analysis (TGA, Fig. S16). It should be pointed out that the NbSSe/NC demonstrates a smaller specific surface area (100 m^2 g^{-1}) compared with NbS_2/NC (125 m^2 g^{-1}), which should be attributed to the doping of heavy Se atoms (Fig. S17).

3.3 Electrochemical Performance of NbSSe/NC Anode

To study the electrochemical properties of the NbSSe/NC nanosheets architecture for Na^+ storage, the cyclic voltammogram (CV) and ex situ characterizations were conducted. As illustrated in the CV curves (Fig. 3a), a sharp strong peak at 1.51 V during the initial cycle is attributed to the Na^+ intercalation into NbSSe/NC interlayers. A board peak at around 0.88 V is attributed to the conversion reaction with the formation of metallic Nb and Na_2S and Na_2Se. At the initial reverse scanning, three anodic peaks at about 1.55, 2.05 and 2.14 V are observed, which correspond to the processes of the reverse conversion reactions and the Na^+ extraction process. Interestingly, the higher peak current density and smaller polarization voltage between conversion reaction can be observed for the NbSSe/NC electrode, further proving the introduction of Se can favorably promote the electrochemical reactivity (Fig. S18) [30]. The subsequent CV curves of NbSSe/NC are almost overlapped, implying a good stability of NbSSe/NC anode after the initial cycle (Fig. S19).

Furthermore, the structural transition and phase evolution of NbSSe/NC during the initial cycle were examined by ex situ XRD, Raman, XPS and HRTEM characterizations. Figure 3b-c shows the ex situ XRD patterns of NbSSe/NC for the initial cycle. Before discharging, the peak at 31.1° could be assigned to (100) crystal planes of NbSSe. When the cell discharges to 0.3 V, this peak negatively shifts to 29.8°, implying the lattice expansion due to the intercalation of Na^+ into NbSSe forming intermediate product of Na_xNbSSe; the new diffraction peaks at 34.8° and 37.5° synchronously emerge, which could be indexed to the formation of Na_2S and Na_2Se interphases, implying the occurrence of the conversion reaction [31, 32]. As the potential decreases to 0.01 V, the characteristic peaks belonging to NbSSe completely disappear. After recharging back to 3.0 V, the (100) peak reappears and shifts back to the pristine position, which suggests this process is reversible. According to the ex situ Raman spectroscopy (Fig. 3d), one can observe that the E_{2g}

(Nb–S) vibration peak of NbSSe tends to decay and shift positively to a higher wavenumber during Na^+ insertion and finally vanishes owing to the consecutive intercalation-conversion phase transition [33]. This peak gradually recovers again during the subsequent charging process, which is in accord with XRD results [34].

The phase evolution upon charging–discharging process was further confirmed by ex situ HRTEM (Fig. 3e-h). The (002) lattice plane space is expanded from ~ 0.65 to ~ 0.85 nm when the Na^+ insertion (Fig. 3e), and materials would subsequently convert into metallic Nb, Na_2S and Na_2Se after discharging to 0.01 V (Fig. 3f-g) [15, 35]. When reversibly charged to 3.0 V, the interlayer structural nanosheets would re-emerge (Fig. 3h). The corresponding mechanisms were also investigated by ex situ XPS. As shown in the S region (Fig. 3i), for the fresh electrode, the doublet characteristic peaks at 161.7 and 162.9 eV represent the $2p_{3/2}$ and $2p_{1/2}$ orbitals of S^{2-} of metal sulfide. After discharging to 0.01 V, a new peak at a lower binding energy of 160.5 eV emerges, which indicates the formation of Na_2S, and a slight peak of S^{2-} is detected, which might be assigned to the existence of Na_xNbSSe [36]. With charging to 3.0 V, the peak of Na_2S disappears and the intensity of S^{2-} peaks recovers again. The similar trend can also be observed in the binding energy of Se $2p$ in the energy shifts and intensities (Fig. 3j), confirming a reversible Na^+ storage capability. The above results reveal that the NbSSe/NC tends to follow an intercalation-conversion reaction during the cycling process, as schematically shown in Fig. 3k.

The electrochemical performance was measured by 2032-type half-cells with the metallic sodium as counter and reference electrode. Figure 4a presents cycling performance of Nb-based electrode at a current density of 0.1 A g^{-1}, where NbSSe/NC electrode can deliver the first discharging and charging capacities of 645.1 and 419.8 mAh g^{-1} with the initial Coulombic efficiency (ICE) of 65.2%, which is much higher than that of NbS_2/NC (51.9%), and NbS_2 nanosheets (47.1%). The increased ICE of NbSSe/NC electrode further demonstrates the improved reversibility, majorly because the bonding energy of Nb–Se bond is weaker than that of Nb–S bond. Accordingly, the NbSSe/NC electrode shows durable cycling stability, where the specific capacity can maintain around 413.5 mAh g^{-1} after 200 cycles with a capacity retention of 96.4% relative to the second-cycle capacity, which outperforms those of the NbS_2/NC (293.6 mAh g^{-1}, 67.6%) and NbS_2 nanosheets (181 mAh g^{-1}, 48.3%). Figures 4b and
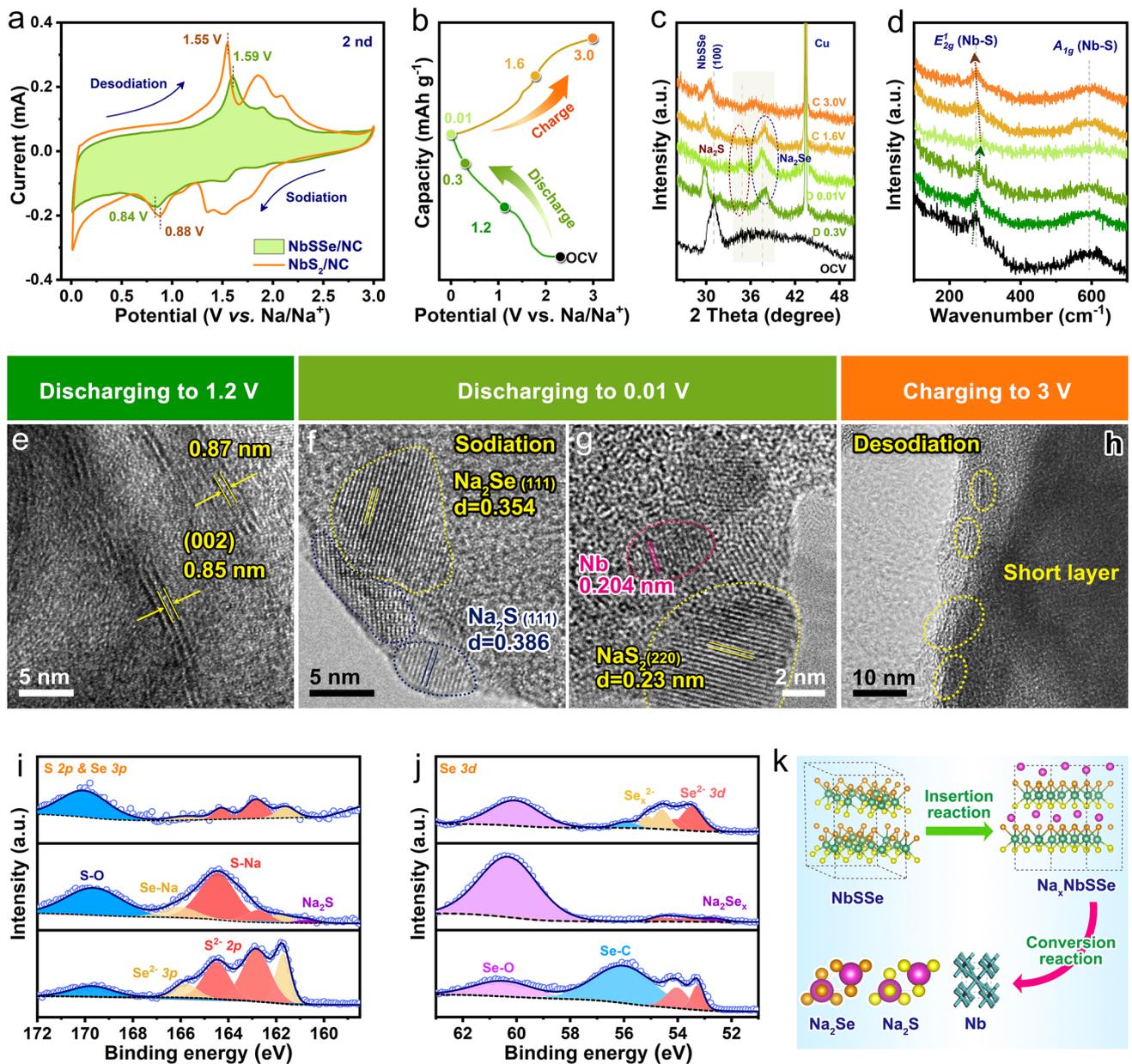
Fig. 3 **a** CV curves during second cycle. **b** Initial charge-discharge curves. **c** Ex situ XRD. **d** Raman pattern coupled with corresponding charge/discharge curves. **e–h** Ex situ HRTEM images at various potentials during initial cycle. **i, j** Ex situ XPS pattern. **k** Schematic diagram of electrochemical mechanism for NbSSe/NC

S20 display the dQ/dV plots of both Nb-based electrodes, where the redox peaks of NbSSe/NC can well maintain even after 200 cycles. In contrast, there is significant variation in the redox peaks for NbS$_2$/NC electrode, which are possibly attributed to the loss of active materials due to the shuttle effect of polysulfides [28].

The rate capability at various current densities is further studied, as shown in Fig. 4c. The NbSSe/NC electrode can deliver the specific capacities of 425.3, 396.2, 356.6, 333.6 and 307.1 mAh g^{-1} at current densities from 0.1 to 2.0 A g^{-1}, respectively, which display a slightly attenuated tendency with the increase in specific current. Notably, even
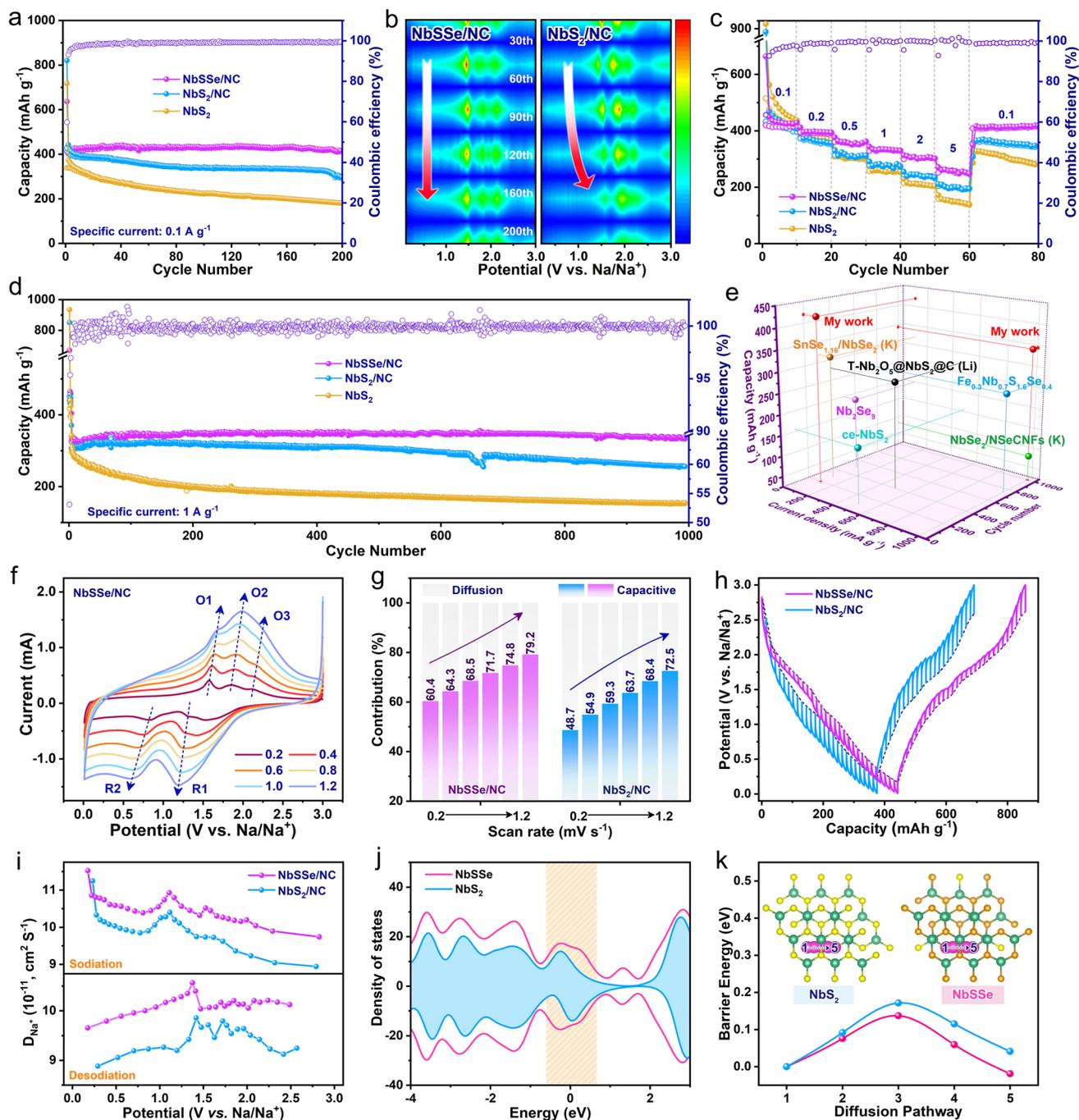
Fig. 4 **a** Cycling performance at 0.1 A g^{-1} and **b** the corresponding dQ/dV curves from the 10th to 200th cycle for NbSSe/NC and NbS$_2$/NC electrode. **c** Rate capability and **d** long-term cycling performance at 1 A g^{-1}. **e** Survey of long-cycling stability of selective Nb-based material electrodes. **f** CV curves at various scan rates from 0.2 to 1.2 mV s^{-1}, **g** normalized contribution ratio of capacitive and diffusion at different scan rates, **h** GITT curves and **i** corresponding Na$^+$ diffusion coefficients of NbSSe/NC and NbS$_2$/NC at 0.1 A g^{-1} after the 10th cycles. **j** Total density of states (DOS). **k** Schematic illustration for the diffusion path of Na$^+$ in the NbS$_2$ and NbSSe, and corresponding diffusion energy barrier curves

at the high rate of 5.0 A g^{-1}, this value can still maintain as high as 262.4 mAh g^{-1}, and the specific capacity can recover to 414.6 mAh g^{-1} when the current density returns

to 0.1 A g^{-1}. In contrast, under the same testing conditions, both NbS$_2$/NC and NbS$_2$ electrodes exhibit a rapid capacity decay from 452.5 to 201.6 mAh g^{-1} and 478.8 to 148.5 mAh

g^{-1}, respectively. Additionally, the stable GCD profiles and slowly increased electrochemical polarization phenomenon of NbSSe/NC with the increasing specific current further confirm the excellent Na^+ capture ability (Fig. S21). To the best of our knowledge, the NbSSe/NC shows improved rate capability relative to the majority of recently reported works for NbS_2-, NbSe_2- and NbSSe-based anodes for Na^+ storage (Fig. S22). The long-term cycling performance was tested at 1.0 A g^{-1}, as shown in Fig. 4d. The reversible capacity of NbSSe/NC can maintain over 347.8 mAh g^{-1} with a capacity retention of 95.6% after 1,000 cycles, being indicative of robust stability (Fig. S23), and is distinctly better than those of the NbS_2/NC (76.1%) and NbS_2 (49.2%). In addition, the NbSSe/NC also delivers excellent cycling stability after rate performance measurements, further implying the highly reversible Na^+ storage behavior (Fig. S24). The excellent cycling performance of NbSSe/NC shows competitive to other reported Nb-based anodes for SIBs (Fig. 4e) [8, 21, 23, 37–40].

3.4 Kinetic Analysis of NbSSe/NC Anode

In order to in-depth shed light on the enhanced Na^+ storage kinetics of the NbSSe/NC anode, the CV measurement at different scan rates was performed (Fig. 4f). As shown in Fig. 4g, the capacitive contribution percentage is gradually increased with enhancing of scan rates, and one can observe that the capacitive-controlled contributions in NbSSe/NC are higher than that of NbS_2/NC at the same scan rate (Figs. S25–S26), demonstrating the improved reaction kinetics in NbSSe/NC anode [41]. The galvanostatic intermittent titration technique (GITT) test was performed to in situ evaluate interfacial reaction resistances of Nb-based electrodes during the sodiation and desodiation process (Figs. 4h-i and S27) [42]. It can be seen that the NbSSe/NC presents a slight voltage hysteresis corresponding to a weak electrochemical polarization. Moreover, the NbSSe/NC shows much higher Na^+ diffusion coefficients (D_{Na}) than NbS_2/NC, uncovering the faster Na^+ diffusion property thanks to the enlarged interlayer space in NbSSe/NC composite. The fast kinetics can be attributed to the improved conductivity, as revealed by electrochemical impedance spectroscopy (EIS) analysis (Fig. S28). The charge transfer resistance (Rct) for NbSSe/NC is reduced value when compared with NbS_2/NC [43]. Moreover, the calculated diffusion coefficient of NbSSe/

NC $(6.35 \times 10^{-10}$ cm^2 $\text{s}^{-1})$ is higher than that of NbS_2/NC $(1.38 \times 10^{-12}$ cm^2 $\text{s}^{-1})$, revealing a speedy Na^+ diffusion in NbSSe/NC. Furthermore, the density of states (DOS) value of NbSSe is higher than that of NbS_2, which indicates the introduction of anion defect can optimize the electronic structure and facilitate electron transfer efficiency, agreeing with the electrical conductivity result (Fig. 4j) [44]. As indicated in Figs. 4k and S29, the diffusion energy profiles simulate the energy barriers of Na^+ migration in the interlayers of both models, where a lower value for NbSSe/NC suggests a positive effect of the enlarged interlayers and anion defects toward the optimization of Na^+ volume-phase diffusion kinetics and thus achieving a favorable rate performance [45].

Based on the above results, the NbSSe/NC presents a set of merits as the anode material for Na^+ storage: (i) the introduction of anion defects presents a cooperative effect on the charge self-regulation, increasing abundant active sites and enhancing intrinsic electrical conductivity; (ii) the formation of weak Nb–Se ionic bonds is prone to separate than Nb–S bands, which is favored to improve the reaction reversibility; (iii) the expended lattice spacing provides broads Na^+ diffusion paths and lowers Na-ion diffusion energy barrier; and iv) besides, the N-doped carbon protect layer is beneficial to relieve the volume expansion and maintain the structural stability. Therefore, these structural and componential merits of NbSSe/NC endow it with fast charge-storage dynamics for achieving high-performance SDIBs.

3.5 Electrochemical Performance Tests in SDIBs

The Na dual-ion full cells were assembled by employing the pre-sodiated NbSSe/NC as anode and expanded graphite (EG) as the cathode, which are schematically presented in Fig. 5a. The structural characteristics and electrochemical performance of EG are shown in Figs. S30–S31 [46]. Figure 5b shows the GCD curves of voltage *vs.* normalized capacity for NbSSe/NC anode and EG cathode. According to the charge balance criterion between individual material levels, the voltage cutoff window is selected between 1.5 and 4.8 V, and the electrode mass ratio of anode/cathode is ~ 1:4 (Fig. S32) [47]. As depicted in Fig. 5c, the dual-ion full cell displays a high reversible capacity of 62 mAh g^{-1} with a capacity retention of 87.1% over 200 cycles at 0.05 A g^{-1}. (The specific capacity is calculated based on the total mass

of anode and cathode.) More importantly, the medium discharge voltage could be stably maintained at 3.70 V during the cycling process (Fig. S33), suggesting their high-work voltage feature. Figure 5d displays the rate performance at the various current density, and the delivered capacities of full cells are 62.5, 59.7, 57.2, 54.6 and 58.8 mAh g^{-1} at the current rates of 0.05, 0.125, 0.25, 0.5 and 1.25 A g^{-1}, respectively. Moreover, the GCD curves at different current densities show low polarization phenomenon (Fig. 5e), verifying the excellent rate ability of full cell. The long-term

cycling stability of full cell at a high current density of 1 A g^{-1} is illustrated in Fig. 5f. After a long-time cycling over 1,000 cycles, the reversible capacity of full cell can be well maintained at 51.7 mAh g^{-1}, corresponding to a high capacity retention of 89.1%. In addition, this device can successfully light up a simple "Wenergy" logo pattern consisting of light-emitting diode (LED) bulbs, which embodies its potential practical value (inset in Fig. 5f). Figure 5g displays the Ragone plot of the Na-DIBs full cell based on the total mass of the anode and the cathode. As a result, the NbSSe/NC//
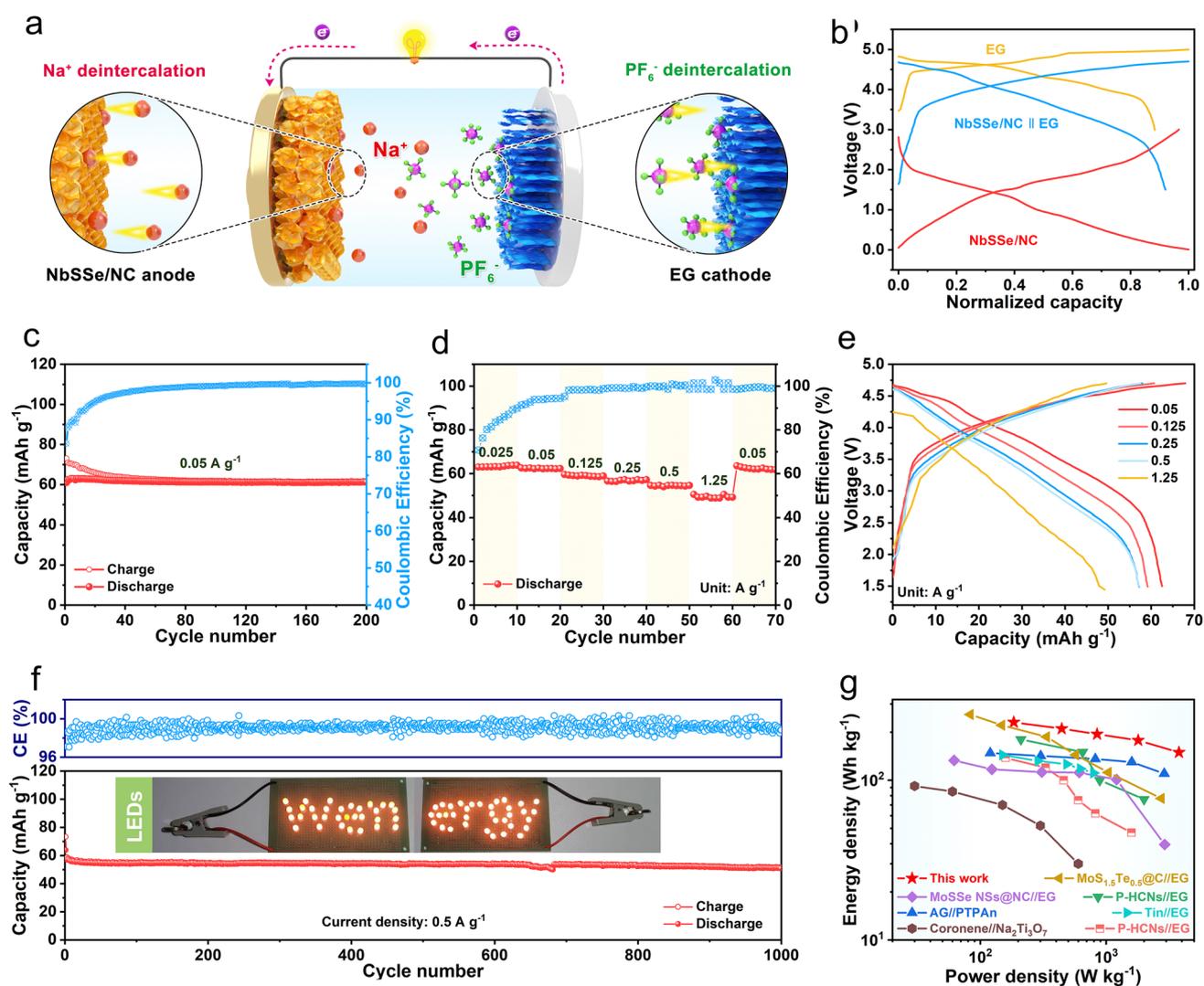
Fig. 5 The electrochemical performance of SDIBs. **a** Schematic diagram of NbSSe/NC//EG full cell. **b** Charge–discharge profiles of NbSSe/NC anode, EG cathode and full cell. **c** Cycling performance and **d** rate capability of the full cells. **e** Galvanostatic charge–discharge voltage profiles of full cell at various rates. **f** Long cycling stability of full cells at 0.5 A g^{-1}. Inset in **f**: The digital photographs of the "Wenergy" logo composing of 64 LEDs light up by two cells. **g** Comparison of the energy density of NbSSe/NC//EG full cell with the reported SDIBs

EG full cells achieve a maximum specific energy density of 230.6 Wh kg^{-1} at a current density of 0.05 A g^{-1}, which is comparable to and even exceeds those of some representative sodium-based dual-ions full batteries reported in the literature (Fig. S34) [3, 48–52]. Additionally, the cycling performance comparison between this work and previously reported SDIBs is displayed in Tables S2 and S3, which indicates its potential feasibility as a high-performance energy storage device for future application.

4 Conclusions

In summary, we reported single-phase NbSSe nanosheets hybrids architecture consisting of N-doped carbon film-modified few-layer sheets as building units. The anionic substitution of Se atoms into the NbS$_2$ lattice would not only broaden interlayer spacing and enhance intrinsic electronic conductivity, but also generate abundant structural defects, and provides rich active sites for Na$^+$ ion storage, significantly promoting the electron/ions migration kinetic, electrochemical reaction reversibility, as well as pseudocapacitive storage effect. With these merits, the as-prepared NbSSe/NC anode can deliver a reversible capacity of as high as 414.6 mAh g^{-1} at 0.1 A g^{-1} over 100 cycles and long-term stable cyclability with 95.6% capacity retention after 1,000 cycles at 1 A g^{-1}. The NbSSe/C was also verified to be practically potential in a full sodium-based dual-ion battery cell by exhibiting a high work voltage and stable capacity output over 1000 cycles, and high energy density of 230.6 Wh kg^{-1}. Such defect engineering strategy in this work provides a new strategy for the construction of high-performance anode materials and highlights their applicability prospects in sodium-based energy storage devices.

References

1. A. Noori, M.F. El-Kady, M.S. Rahmanifar, R.B. Kaner, M.F. Mousavi, Towards establishing standard performance metrics for batteries, supercapacitors and beyond. Chem. Soc. Rev. **48**, 1272–1341 (2019). https://doi.org/10.1039/c8cs00581h

2. T. Placke, A. Heckmann, R. Schmuch, P. Meister, K. Beltrop et al., Perspective on performance, cost, and technical challenges for practical dual-ion batteries. Joule **2**, 2528–2550 (2018). https://doi.org/10.1016/j.joule.2018.09.003

3. Y. Liu, X. Hu, J. Li, G. Zhong, J. Yuan et al., Carbon-coated MoS$_{1.5}$Te$_{0.5}$ nanocables for efficient sodium-ion storage in non-aqueous dual-ion batteries. Nat. Commun. **13**, 663 (2022). https://doi.org/10.1038/s41467-022-28176-0

4. C. Jiang, L. Xiang, S. Miao, L. Shi, D. Xie et al., Flexible interface design for stress regulation of a silicon anode toward highly stable dual-ion batteries. Adv. Mater. **32**, e1908470 (2020). https://doi.org/10.1002/adma.201908470

5. P. Qin, M. Wang, N. Li, H. Zhu, X. Ding et al., Bubble-sheet-like interface design with an ultrastable solid electrolyte layer for high-performance dual-ion batteries. Adv. Mater. **29**, 1606805 (2017). https://doi.org/10.1002/adma.201606805

6. J. Zhou, Y. Shen, F. Lv, W. Zhang, F. Lin et al., Ultrathin metallic NbS$_2$ nanosheets with unusual intercalation mechanism for ultra-stable potassium-ion storage. Adv. Funct. Mater. **32**, 2204495 (2022). https://doi.org/10.1002/adfm.202204495

7. H. Zhang, J. Cheng, H. Wang, Z. Huang, Q. Zheng et al., Initiating VB-group laminated NbS2 electromagnetic wave absorber toward superior absorption bandwidth as large as 6.48 GHz through phase engineering modulation. Adv. Funct. Mater. **32**, 2108194 (2021). https://doi.org/10.1002/adfm.202108194

8. J. Zhang, C. Du, Z. Dai, W. Chen, Y. Zheng et al., NbS2 nanosheets with M/Se (M = Fe Co, Ni) codopants for Li+ and Na+ storage. ACS Nano **11**, 10599–10607 (2017). https://doi.org/10.1021/acsnano.7b06133

9. Z. Wang, J. Huang, Z. Guo, X. Dong, Y. Liu et al., A metal-organic framework host for highly reversible dendrite-free zinc metal anodes. Joule **3**, 1289–1300 (2019). https://doi.org/10.1016/j.joule.2019.02.012

10. Y.R. Luo, *Comprehensive Handbook of Chemical Bond Energies* (CRC Press, London, 2007)

11. S. Nanda, A. Bhargav, A. Manthiram, Anode-free, lean-electrolyte lithium-sulfur batteries enabled by tellurium-stabilized lithium deposition. Joule **4**, 1121–1135 (2020). https://doi.org/10.1016/j.joule.2020.03.020

12. H. Li, R. Gao, B. Chen, C. Zhou, F. Shao et al., Vacancy-rich MoSSe with sulfiphilicity-lithiophilicity dual function for kinetics-enhanced and dendrite-free Li-S batteries. Nano Lett. **22**, 4999–5008 (2022). https://doi.org/10.1021/acs.nanolett.2c01779

13. Y. Huang, Z. Wang, M. Guan, F. Wu, R. Chen, Toward rapid-charging sodium-ion batteries using hybrid-phase molybdenum sulfide selenide-based anodes. Adv. Mater. **32**, 2003534 (2020). https://doi.org/10.1002/adma.202003534

14. H. Fan, X. Wang, H. Yu, Q. Gu, S. Chen et al., Enhanced potassium ion battery by inducing interlayer anionic ligands in $MoS_{1.5}Se_{0.5}$ nanosheets with exploration of the mechanism. Adv. Energy Mater. **10**, 1904162 (2020). https://doi.org/10.1002/aenm.201904162

15. T. Wang, D. Legut, Y. Fan, J. Qin, X. Li et al., Building fast diffusion channel by constructing metal sulfide/metal selenide heterostructures for high-performance sodium ion batteries anode. Nano Lett. **20**, 6199–6205 (2020). https://doi.org/10.1021/acs.nanolett.0c02595

16. S. Yao, J. Cui, J. Huang, Z. Lu, Y. Deng et al., Novel 2D Sb_2S_3 nanosheet/CNT coupling layer for exceptional polysulfide recycling performance. Adv. Energy Mater. **8**, 1800710 (2018). https://doi.org/10.1002/aenm.201800710

17. Z. Shen, Z. Zhang, M. Li, Y. Yuan, Y. Zhao et al., Rational design of a $Ni_3N_{0.85}$ electrocatalyst to accelerate polysulfide conversion in lithium-sulfur batteries. ACS Nano **14**, 6673–6682 (2020). https://doi.org/10.1021/acsnano.9b09371

18. S. Zhang, F. Ling, L. Wang, R. Xu, M. Ma et al., An open-ended Ni_3S_2-Co_9S_8 heterostructures nanocage anode with enhanced reaction kinetics for superior potassium-ion batteries. Adv. Mater. **34**, e2201420 (2022). https://doi.org/10.1002/adma.202201420

19. H. Lu, S. Ghosh, N. Katyal, V.S. Lakhanpal, I.R. Gearba-Dolocan et al., Synthesis and dual-mode electrochromism of anisotropic monoclinic $Nb_{12}O_{29}$ colloidal nanoplatelets. ACS Nano **14**, 10068–10082 (2020). https://doi.org/10.1021/acsnano.0c03283

20. Y. Huan, J. Shi, X. Zou, Y. Gong, C. Xie et al., Scalable production of two-dimensional metallic transition metal dichalcogenide nanosheet powders using NaCl templates toward electrocatalytic applications. J. Am. Chem. Soc. **141**, 18694–18703 (2019). https://doi.org/10.1021/jacs.9b06044

21. M. Chen, L. Wang, X. Sheng, T. Wang, J. Zhou et al., An ultrastable nonaqueous potassium-ion hybrid capacitor. Adv. Funct. Mater. **30**, 2004247 (2020). https://doi.org/10.1002/adfm.202004247

22. D. Yang, Z. Liang, C. Zhang, J.J. Biendicho, M. Botifoll et al., $NbSe_2$ meets C_2N: A 2D–2D heterostructure catalysts as multifunctional polysulfide mediator in ultra-long-life lithium-sulfur batteries. Adv. Energy Mater. **11**, 2101250 (2021). https://doi.org/10.1002/aenm.202101250

23. L. Zhou, X. Gao, T. Du, H. Gong, L. Liu et al., Two-dimensional NbSSe as anode material for low-temperature sodium-ion batteries. Chem. Eng. J. **435**, 134838 (2022). https://doi.org/10.1016/j.cej.2022.134838

24. Y. Bai, Y. Liu, C. Ma, K. Wang, J. Chen, Neuron-inspired design of high-performance electrode materials for sodium-ion batteries. ACS Nano **12**, 11503–11510 (2018). https://doi.org/10.1021/acsnano.8b06585

25. Z. Shi, W. Kang, J. Xu, J. Sun, M. Jiang et al., Hierarchical nanotubes assembled from MoS_2-carbon monolayer sandwiched superstructure nanosheets for high-performance sodium ion batteries. Nano Energy **22**, 27–37 (2016). https://doi.org/10.1016/j.nanoen.2016.02.009

26. Y. Liu, Y. Zhai, N. Wang, Y. Zhang, Z. Lu et al., Ultrathin $MoSe_2$ nanosheets confined in N-doped macroporous carbon frame for enhanced potassium ion storage. ChemistrySelect **5**, 2412–2418 (2020). https://doi.org/10.1002/slct.202000116

27. D. Cheng, L. Yang, R. Hu, J. Liu, R. Che et al., Sn-C and Se-C co-bonding SnSe/few-layered graphene micro-nano structure: route to a densely compacted and durable anode for lithium/sodium-ion batteries. ACS Appl. Mater. Interfaces **11**, 36685–36696 (2019). https://doi.org/10.1021/acsami.9b12204

28. M. Yan, Z. Zhao, T. Wang, R. Chen, C. Zhou et al., Synergistic effects in ultrafine molybdenum-tungsten bimetallic carbide hollow carbon architecture boost hydrogen evolution catalysis and lithium-ion storage. Small **18**, e2203630 (2022). https://doi.org/10.1002/smll.202203630

29. W. Xue, Z. Shi, L. Suo, C. Wang, Z. Wang et al., Intercalation-conversion hybrid cathodes enabling Li-S full-cell architectures with jointly superior gravimetric and volumetric energy densities. Nat. Energy **4**, 374–382 (2019). https://doi.org/10.1038/s41560-019-0351-0

30. R. Xu, Y. Yao, H. Wang, Y. Yuan, J. Wang et al., Unraveling the nature of excellent potassium storage in small-molecule Se@peapod-like N-doped carbon nanofibers. Adv. Mater. **32**, e2003879 (2020). https://doi.org/10.1002/adma.202003879

31. Y. Wang, Y. Lai, J. Chu, Z. Yan, Y. Wang et al., Tunable electrocatalytic behavior of sodiated MoS_2 active sites toward efficient sulfur redox reactions in room-temperature Na-S batteries. Adv. Mater. **33**, e2100229 (2021). https://doi.org/10.1002/adma.202100229

32. Z. Yan, Y. Liang, J. Xiao, W. Lai, W. Wang et al., A high-kinetics sulfur cathode with a highly efficient mechanism for superior room-temperature Na-S batteries. Adv. Mater. **32**, e1906700 (2020). https://doi.org/10.1002/adma.201906700

33. Y. Tan, S. Li, X. Zhao, Y. Wang, Q. Shen et al., Unexpected role of the interlayer "dead Zn^{2+}" in strengthening the nanostructures of VS_2 cathodes for high-performance aqueous Zn-ion storage. Adv. Energy Mater. **12**, 2104001 (2022). https://doi.org/10.1002/aenm.202104001

34. G. Yang, Q. Li, K. Ma, C. Hong, C. Wang, The degradation mechanism of vanadium oxide-based aqueous zinc-ion batteries. J. Mater. Chem. A **8**, 8084–8095 (2020). https://doi.org/10.1039/d0ta00615g

35. S. Zhang, Y. Yao, X. Jiao, M. Ma, H. Huang et al., Mo_2N-W_2N heterostructures embedded in spherical carbon superstructure as highly efficient polysulfide electrocatalysts for stable room-temperature Na-S batteries. Adv. Mater. **33**, e2103846 (2021). https://doi.org/10.1002/adma.202103846

36. Q. Pan, Q. Zhang, F. Zheng, Y. Liu, Y. Li et al., Construction of MoS_2/C hierarchical tubular heterostructures for high-performance sodium ion batteries. ACS Nano **12**, 12578–12586 (2018). https://doi.org/10.1021/acsnano.8b07172

37. Q. Peng, F. Ling, H. Yang, P. Duan, R. Xu et al., Boosting potassium storage performance via construction of $NbSe_2$-based misfit layered chalcogenides. Energy Stor. Mater. **39**, 265–270 (2021). https://doi.org/10.1016/j.ensm.2021.04.032

38. X. Ou, X. Xiong, F. Zheng, C. Yang, Z. Lin et al., In situ X-ray diffraction characterization of NbS_2 nanosheets as the anode material for sodium ion batteries. J. Power Sourc. **325**, 410–416 (2016). https://doi.org/10.1016/j.jpowsour.2016.06.055

39. C. Pan, J. Kang, Q. Xie, Q. Li, W. Yang et al., T-Nb_2O_5@NbS_2@C composites based on the intercalation-conversion mechanism as an anode material for Li-ion batteries. ACS Appl. Energy Mater. **4**, 12365–12373 (2021). https://doi.org/10.1021/acsaem.1c02165

40. X. Wu, B. Wu, H. Wang, Q. Zhuang, Z. Xiong et al., Synthesis of flower-Like Nb_2Se_9 as high-performance anode materials for lithium-ion and sodium-ion batteries. Energy Fuels **35**, 11563–11571 (2021). https://doi.org/10.1021/acs.energyfuels.1c01258

41. K. Yang, Q. Liu, Y. Zheng, H. Yin, S. Zhang et al., Locally ordered graphitized carbon cathodes for high-capacity dual-ion batteries. Angew. Chem. Int. Ed. **60**, 6326–6332 (2021). https://doi.org/10.1002/anie.202016233

42. X. Pan, B. Xi, H. Lu, Z. Zhang, X. An et al., Molybdenum oxynitride atomic nanoclusters bonded in nanosheets of N-doped carbon hierarchical microspheres for efficient sodium storage. Nano-Micro Lett. **14**, 163 (2022). https://doi.org/10.1007/s40820-022-00893-7

43. Z. Song, L. Miao, L. Ruhlmann, Y. Lv, D. Zhu et al., Lewis pair interaction self-assembly of carbon superstructures harvesting high-energy and ultralong-life zinc-ion storage. Adv. Funct. Mater. **32**, 2208049 (2022). https://doi.org/10.1002/adfm.202208049

44. J. Sun, Z. Zhang, G. Lian, Y. Li, L. Jing et al., Electron-injection and atomic-interface engineering toward stabilized defected 1T-rich MoS_2 as high rate anode for sodium storage. ACS Nano **16**, 12425–12436 (2022). https://doi.org/10.1021/acsnano.2c03623

45. B. Chen, L. Yang, X. Bai, Q. Wu, M. Liang et al., Heterostructure engineering of core-shelled Sb@Sb_2O_3 encapsulated in 3D N-doped carbon hollow-spheres for superior sodium/potassium storage. Small **17**, e2006824 (2021). https://doi.org/10.1002/smll.202006824

46. D. Yu, Q. Zhu, L. Cheng, S. Dong, X. Zhang et al., Anion solvation regulation enables long cycle stability of graphite cathodes. ACS Energy Lett. **6**, 949–958 (2021). https://doi.org/10.1021/acsenergylett.1c00043

47. D. Yu, W. Luo, H. Gu, K. Li, J. Liang et al., Subnano-sized tellurium@nitrogen/phosphorus co-doped carbon nanofibers as anode for potassium-based dual-ion batteries. Chem. Eng. J. **454**, 139908 (2023). https://doi.org/10.1016/j.cej.2022.139908

48. B. Liu, Y. Liu, X. Hu, G. Zhong, J. Li et al., N-doped carbon modifying MoSSe nanosheets on hollow cubic carbon for high-performance anodes of sodium-based dual-ion batteries. Adv. Funct. Mater. **31**, 2101066 (2021). https://doi.org/10.1002/adfm.202101066

49. X. Wang, S. Wang, K. Shen, S. He, X. Hou et al., Phosphorus-doped porous hollow carbon nanorods for high-performance sodium-based dual-ion batteries. J. Mater. Chem. A **8**, 4007–4016 (2020). https://doi.org/10.1002/adfm.202101066

50. X. Wang, M. Hou, Z. Shi, X. Liu, I. Mizota et al., Regulate phosphorus configuration in high P-doped hard carbon as a superanode for sodium storage. ACS Appl. Mater. Interfaces **13**, 12059–12068 (2021). https://doi.org/10.1021/acsami.0c23165

51. J. Chen, Y. Peng, Y. Yin, Z. Fang, Y. Cao et al., A desolvation-free sodium dual-ion chemistry for high power density and extremely low temperature. Angew. Chem. Int. Ed. **60**, 23858–23862 (2021). https://doi.org/10.1002/anie.202110501

52. S. Dong, Z. Li, I.A. Rodríguez-Pérez, H. Jiang, J. Lu et al., A novel coronene//$Na_2Ti_3O_7$ dual-ion battery. Nano Energy **40**, 233–239 (2017). https://doi.org/10.1016/j.nanoen.2017.08.022